Acoustic Tunable Battery-Free Implants Based on Sustainable Triboelectric Nanogenerators With Metal-Polymer Intermixing Layers

Youngwook Chung, Hongwei Yuan, Ze Wang, Jang-Mook Jeong, Byung-Joon Park, Joon-Ha Hwang, Su-Jeong Suh, Byung-Ok Choi, Hyun-moon Park, Young-Jun Kim,* Keren Dai,* and Sang-Woo Kim*

Ultrasound-driven triboelectric nanogenerators (US-TENGs) offer an innovative solution for transcutaneous power transfer, with the potential to enable battery-free, permanently implantable electronics. However, research to date has primarily demonstrated only fragmentary functionalities for these applications. This work presents the simultaneous transmission of acoustic power and precise acoustic information using a double-electrode US-TENG, enabling a battery-free implant controlled via ultrasound. High and sustained output from a US-TENG is crucial for operating the versatile system; therefore, a novel triboelectric membrane with a top electrode incorporating a gold-polymer intermixing layer has been designed. Reversible micro-cracks form in the intermixing layer, ensuring electrical connectivity under high-frequency strain. In vivo experiments confirm that the system is biocompatible and can be reliably operated inside living rats. These achievements represent a significant step toward realizing multifunctional implantable electronics that can be reliably powered and controlled by ultrasound.

1. Introduction

Implantable electronics enable various physiological therapies that extend beyond the scope of pharmacological approaches. Many implantable electronic devices depend on batteries with limited lifespans, leading to periodic surgeries and constraints on device size.[1,2] There is a growing demand for a new generation of battery-free implants that incorporate sustainable power generation modules.[3–5] Triboelectric nanogenerators (TENGs) have garnered attention for their ability to harvest various forms of in vivo mechanical energy to power implantable electronics; however, the limited mechanical energy available within the body presents a challenge in developing battery-free implants.[6–11] Recent research has shown that an ultrasound-driven triboelectric nanogenerator (US-TENG), which harvests electrical energy from microscopic vibrations of a triboelectric membrane, can power a battery-free implant for treating intractable diseases.[12] Another study reported that a US-TENG enables acoustic signal communication.[13] Despite these advances, previous studies have been limited to implementing fragmentary functionalities, and simultaneous acoustic power transfer and communication have not yet been realized. Achieving high and sustained power generation is essential for powering an implant while transmitting accurate signals, necessitating a profound understanding of US-TENGs and their operational conditions.

US-TENGs harvest ultrasound energy transmitted through the body, which contains various tissues composed of more than 65% water.[14] The body, acting as both a conductor and a dielectric with high permittivity (water: ≈80), can couple with external electric fields.[15] Various energy transmission technologies, such as inductive coupling, magnetoelectric coupling, and body-coupled transmission, face limitations in terms of

Y. Chung, J.-M. Jeong, J.-H. Hwang, S.-J. Suh, Y.-J. Kim
School of Advanced Materials Science and Engineering
Sungkyunkwan University
Suwon 16419, Republic of Korea
E-mail: kimyjun@skku.edu
Y. Chung, J.-M. Jeong, J.-H. Hwang, H.-moon Park, S.-W. Kim
Research and Development Center
Energymining Co., Ltd
Suwon 16226, Republic of Korea
E-mail: kimsw1@yonsei.ac.kr

The ORCID identification number(s) for the author(s) of this article can be found under https://doi.org/10.1002/aenm.202403712

DOI: 10.1002/aenm.202403712

H. Yuan, Z. Wang, K. Dai
School of Mechanical Engineering
Nanjing University of Science and Technology
Nanjing 210094, China
E-mail: dkr@njust.edu.cn
B.-J. Park, S.-W. Kim
Department of Materials Science and Engineering
Center for Human-oriented Triboelectric Energy Harvesting
Yonsei University
Seoul 03722, Republic of Korea
B.-O. Choi
Department of Neurology, Samsung Medical Center
Sungkyunkwan University School of Medicine
Seoul 06351, Republic of Korea

**ADVANCED
SCIENCE NEWS**
www.advancedsciencenews.com

**ADVANCED
ENERGY
MATERIALS**
www.advenergymat.de

transmission efficiency, method, and distance due to the body's unique environment.[16–18] Likewise, TENGs, which generate current via an electric field created by triboelectric charges, have been reported to be affected by environmental factors, potentially leading to either amplified output power or energy loss.[19,20] This suggests that in vivo TENGs, especially those driven by ultrasound, may exhibit different behaviors compared to conventional TENGs. In a previous study investigating the structural factors for a US-TENG, the output power discrepancy between the double-electrode and single-electrode modes was less pronounced than in conventional TENGs;[21] however, the underlying reasons for this observation remain unclear.

Furthermore, there are distinct differences in the operational mechanisms between US-TENGs and conventional contact-mode TENGs.[22,23] US-TENGs harvest energy through micro-vibrations at high frequencies above 20 kHz, with the magnitude of membrane displacement directly proportional to the output power.[24,25] Therefore, complex material design for higher and more sustainable power generation is required from a different perspective than conventional TENGs. This requires i) maximizing the vibrational displacement induced by the ultrasound-structure interaction and ii) adhesion stability between each layer, including the triboelectric layer, electrode, and encapsulation. A previous study reported improving ultrasound transmission efficiency by adjusting the acoustic impedance of the membrane layers,[26] and studies have reported using various electrode membranes for the double-electrode mode;[13,27] however, a membrane design that considers all of these complex factors has not yet been reported.

In this work, we present a sustainable powering double-electrode US-TENG (DUS-TENG) that can achieve both acoustic power transfer and precise information communication, enabling the generation of neurostimulation pulses tunable via ultrasound. Our results indicate that the energy-loss return gate effect[20] can occur through the body and that the double-electrode mode can activate the modulation circuit independently, whereas the single-electrode mode cannot initiate it without this effect. To ensure both high and sustained output in the double-electrode mode, we introduce a highly stable oscillating membrane with a top electrode, where gold (Au) nanoparticles are intermixed within styrene-ethylene-butylene-styrene (SEBS) layers attached to a triboelectric membrane. Reversible microcracks form in the intermixing layer, ensuring electrical connectivity under high-frequency strain. We demonstrate the reliable in vivo operation of the proposed system using the DUS-TENG, which generates neurostimulation pulses with tunable parameters such as frequency, amplitude, and width via ultrasound. These findings highlight the potential feasibility of battery-free and permanently implantable electronics fully controlled by ultrasound.

2. Results

2.1. Design and Application of the DUS-TENG

Figure 1a and Figure S1 (Supporting Information), represent a battery-free neurostimulation system through simultaneous acoustic power transfer and communication using the DUS-TENG. The DUS-TENG harvests ultrasound en-

ergy and generates an alternating current (AC) signal. The power modulation circuit converts the AC signal to monophasic pulses that can stimulate nerves for treating neuropathy or physiological dysfunctions. Simultaneously, it can receive binary signals to adjust the pulse parameters, including amplitude, frequency, and width. This allows adjustable and personalized neurostimulation depending on the body conditions, avoiding adaptation and habituation of nerves.[28,29]

Figure 1b shows the design of the DUS-TENG. The DUS-TENG is a double-electrode mode TENG, driven by the vibration of an integrated membrane that comprises a triboelectric membrane and a strain-durable electrode. We combined a thin (≈25 μm) perfluoroalkoxy (PFA) membrane with a flexible electrode that contains SEBS layers confining Au nanoparticles in the middle. The Au nanoparticles form a nanomembrane (≈45 nm thickness) within the SEBS layers, acting as a top electrode that oscillates in phase with the PFA membrane. The SEBS layers, which have self-adhesive properties, were connected via exposed faces between the Au nanoparticles.[30] PFA exhibits high tribonegative properties, but its low surface energy hinders its adhesion to other layers.[31] A self-assembly monolayer (SAM) based on the phenyl group was formed on the PFA surface to facilitate strong adhesion with the SEBS.[32] Under 20 kHz ultrasound irradiation, the membrane vibrates, inducing an alternating current in the external circuit through contact electrification between the PFA and Au/Cu electrode on the FR-4 printed circuit board (PCB) and the electrostatic induction phenomenon.[33] The modulation circuit was connected to the DUS-TENG to receive power and data from the TENG's output, which allowed for the generation of controllable pulses. The entire system is encapsulated using SEBS, which protects internal components from biofluids. The detailed fabrication processes of the integrated membrane and the DUS-TENG are shown in Figures S2 and S3 (Supporting Information).

Figure 1c illustrates the operating mechanism of the DUS-TENG under ultrasound irradiation. Initially, the structure of DUS-TENG is in the form of a capacitor, with a dielectric layer between the Au nanomembrane and the Au/Cu electrode. When the membrane vibrates under ultrasound irradiation, the triboelectric phenomenon occurs between the PFA and the bottom electrode, leading to negative charges moving toward the inner surface of the PFA. As the membrane separates, the electrical potential of the bottom electrode increases relative to the top electrode, releasing holes and resulting in a current flow from the bottom to the top electrode. After the membrane makes contact again, the electrical potential decreases, creating a reverse current. The ultrasound waves repeatedly induce the contact-separation process, resulting in the formation of a current waveform at a frequency of 20 kHz (Note S1; Figures S4 and S5, Supporting Information).[34,35] Given that the displacement of the membrane relative to the bottom electrode causes a potential difference between the electrodes, the top electrode should oscillate in phase with the PFA membrane

Serving as a power source for implantable electronics, the DUS-TENG is designed to supply power to the circuit independently of external electrical systems.[36] In an electrically isolated system, unconnected to earth ground, the double-electrode TENG generates an output current 9.6 times greater
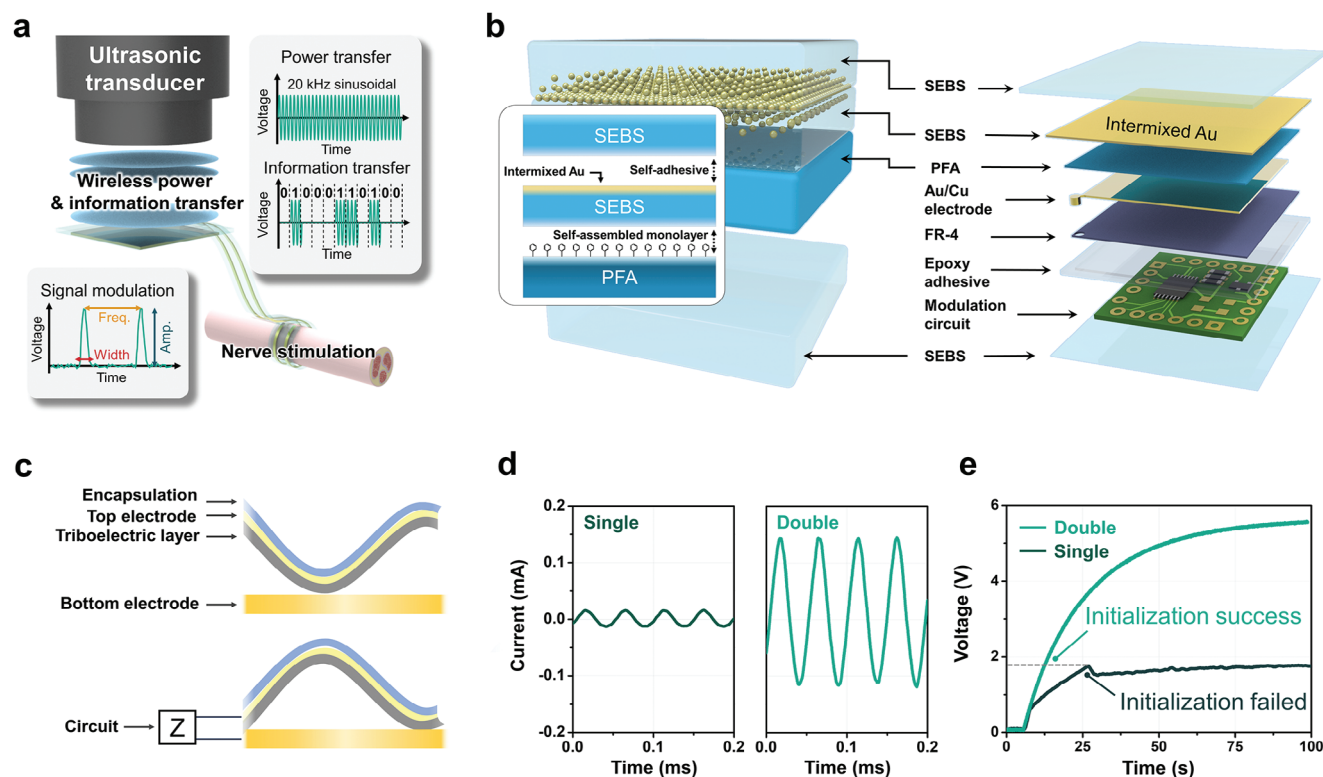
Figure 1. Design and application of the DUS-TENG. a) Schematic illustration representing the simultaneous wireless power and information transfer system using the DUS-TENG. b) Exploded view of the DUS-TENG combined with the modulation circuit. c) Working mechanism of the DUS-TENG. d) Output differences between single and double-electrode TENGs. e) Charging curves of the energy-storage capacitor using the single and double-electrode TENGs.

than that of the single-electrode TENG (Figure 1d). The double-electrode TENG could charge the energy storage capacitor to the required voltage, ≈1.8 V, and successfully drive the microcontroller (Figure 1e). By contrast, the single-electrode TENG failed to charge the capacitor to the required voltage and could not drive the microcontroller. Consequently, the vibrating double-electrode is crucial for enabling practical circuit operation in US-TENGs.

2.2. Electrical System Analysis of US-TENGs with Single and Double-Electrodes

To investigate the necessity of the double-electrode structure in US-TENGs, we conducted an in-depth analysis of the TENG's electrical system based on the electrode configuration. In a low-frequency environment, the double-electrode TENG exhibited a current output 5.9 times higher than that of the single-electrode TENG (Figure S6, Supporting Information). However, during in vitro measurements, US-TENGs exhibited minimal differences in output between double and single-electrode structures (Figure S7, Supporting Information). When operating a TENG, energy loss occurs through dielectric layers; however, in water-rich environments with high dielectric polarization, a return gate can form to compensate for this energy loss (Figure S8, Supporting Information).[20] Accordingly, when ultrasound energy is transmitted through a medium with sig-

nificantly high relative permittivity (water or living body), the energy loss in the single-electrode TENG forms a return gate through the medium and the transducer. This induces a substantial potential difference in its electrode without a paired one, as shown in the finite element analysis (FEA) result (**Figure 2a**).

However, ensuring that US-TENGs can operate independently of external factors necessitates excluding the return gate effect. We simulated an electrically isolated environment by inserting an insulating layer between the transducer and the TENG. The presence of an insulating layer between the TENG and the transducer inhibits the formation of a return gate in the TENGs (Figure 2b,c). Under these conditions, a single-electrode TENG operates without the return gate, leading to a significant decrease in output (FEA result; potential difference in the blue region). However, employing a double-electrode TENG guarantees that the output remains unaffected in an isolated environment, attributable to the formation of electric fields in opposite directions within each electrode. (FEA result; potential difference between the blue and red region). To examine the influence of isolation degree on the return gate effect, we assessed the variation in output as a function of the insulating layer's thickness. In a partially isolated system (featuring an insulating layer of 0.1 mm thickness), the two structures exhibited a 50% difference in the current output. With an increase in thickness, this discrepancy intensified, reaching a 666% difference in a fully isolated system (insulating layer of 5 mm thickness) (Figure 2d).
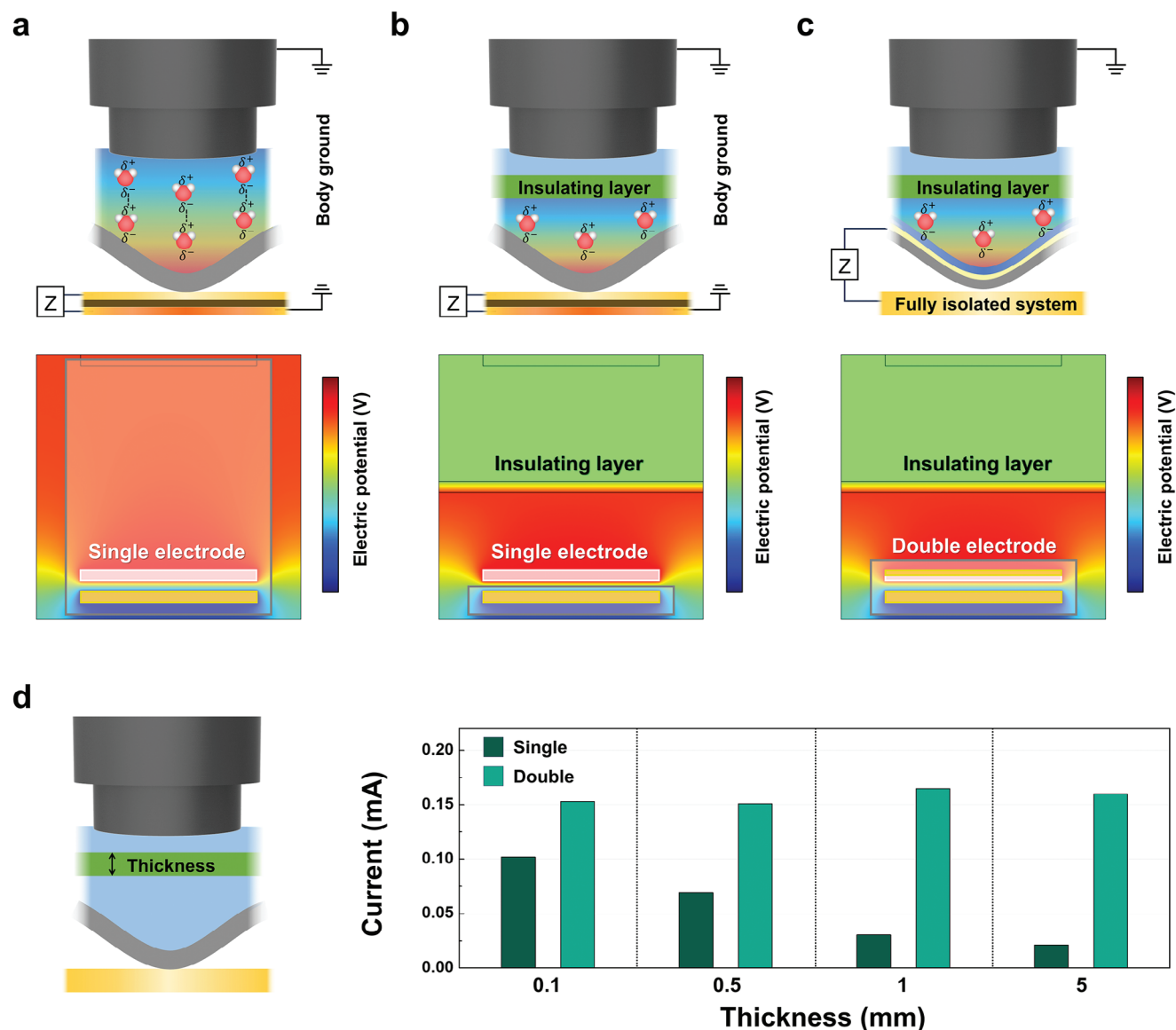
ADVANCED
SCIENCE NEWS

www.advancedsciencenews.com

**ADVANCED
ENERGY
MATERIALS**

www.advenergymat.de

Figure 2. Electrical system analysis of US-TENGs with single and double-electrodes. a–c) Schematic illustrations and FEM simulation results for electrical potential of a single-electrode US-TENG with return gate formed a), a single-electrode US-TENG without return gate formed b), and a double-electrode US-TENG c). d) Output differences between single and double-electrode modes based on degree of isolation.

Consequently, the double-electrode US-TENG exhibited a 24-fold increase in energy conversion efficiency compared to the single-electrode device in a fully isolated system (Figure S9, Supporting Information).

2.3. Material Analysis of the Intermixed Electrode

Next, we designed and analyzed the integrated membrane's capacity to preserve the double-electrode structure under ultrasound irradiation. To confirm the structure of the fabricated integrated membrane, we performed structural analysis using field emission scanning electron microscopy (FE-SEM) with energy dispersive x-ray spectroscopy (EDS) (**Figure 3a**; Figure S10, Supporting Information). The cross-sectional view of the fabricated

membrane revealed distinct layers. A fluorine-rich (blue dots) PFA layer was combined with a carbon-rich (red dots) SEBS layer, composed entirely of saturated hydrocarbons. The Au interlayer (yellow dots) was observed between the SEBS layers. The bottom SEBS layer is an adhesion layer, forming a thin layer of ≈3 µm, and the top SEBS layer serves as an encapsulation layer that protects the device from biofluids, forming a thick layer of ≈15 µm. To confirm the strong adhesion between layers, we conducted T-peel tests to measure their adhesive strength (Figure 3b,c). The Au-confined SEBS layers showed strong interconnectivity through the Au interlayer due to the self-adhesive nature of SEBS. The peel strength of the encapsulation in the Au-confined SEBS layers was found to be 0.17 N mm⁻¹, 25 times greater than that of the conventional polydimethylsiloxane (PDMS)-based Au interlayer. Furthermore, the application of

ADVANCED
SCIENCE NEWS

www.advancedsciencenews.com

ADVANCED
ENERGY
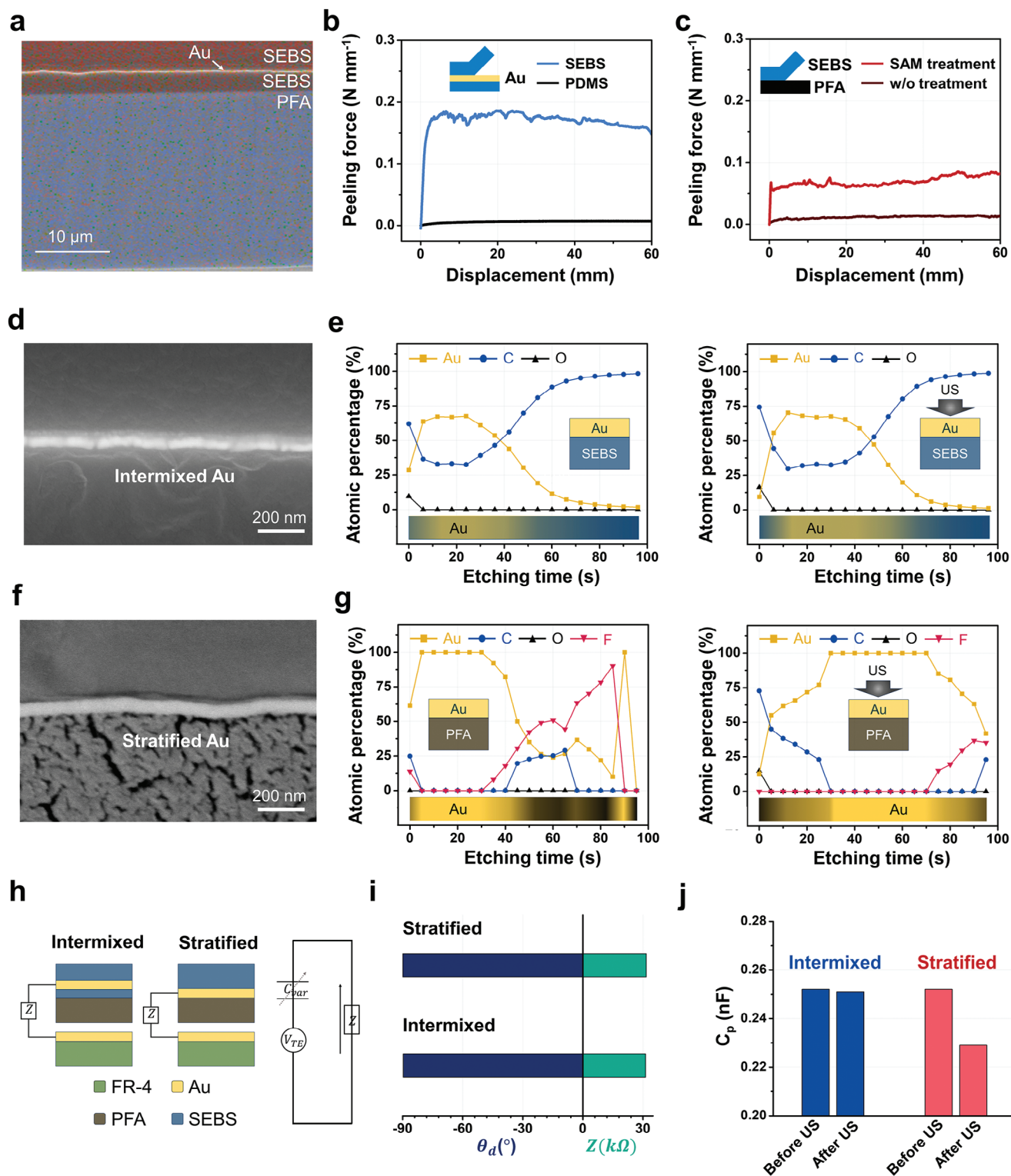**MATERIALS**

www.advenergymat.de

Figure 3. Material analysis of the intermixed electrode. a) Cross-sectional FE-SEM image of the integrated membrane with EDS component mapping for C, F, and Au atoms. b) Comparison of adhesion strength between SEBS and PDMS-based electrodes. c) Comparison of SEBS and PFA adhesion with and without surface treatment. d) Enlarged cross-sectional FE-SEM image representing the intermixed Au between SEBS layers. e) XPS depth profile analysis of the Au nanoparticles on SEBS before and after HIU irradiation. f) Enlarged cross-sectional FE-SEM image representing the stratified Au between PFA and SEBS layers. g) XPS depth profile analysis of the Au nanoparticles on PFA before and after HIU irradiation. h) Simplified electrical modeling of US-TENGs with intermixed and stratified structures. i) Impedance analysis of US-TENGs with intermixed and stratified structures. j) Capacitance changes before and after HIU in intermixed and stratified structures.

SAM treatment on PFA resulted in a 5.7 times increase in adhesive strength with the SEBS layer compared to the untreated sample.

Figure 3d shows the enlarged image centered on the Au interlayer between SEBS layers. The bright line indicates the formation of the conformal Au nanomembrane while the faint yellow lines show that the Au nanoparticles are penetrating and intermixing within the SEBS layer. X-ray photoelectron spectroscopy (XPS) depth profile analysis was performed to investigate how Au nanoparticles are formed at the interface (Figure 3e). We observed the Au-SEBS intermixed region where the atomic percentage of metal (28.5% Au) and SEBS (61.9% C) gradually changed to 67.5% Au and 32.5% C, and subsequently, the Au ratio decreased with etching time. To check the durability of the intermixed region as the operation of the DUS-TENG, we further performed the XPS depth profiling after high-intensity ultrasound (HIU) irradiation (3 W cm^2, 30 min).[35] The Au nanoparticles within the intermixed region remained intact, even under severe conditions. In contrast, when Au nanoparticles were directly deposited on the triboelectric layer, the Au nanoparticles were not intermixing in the polymer layer (Figure 3f). The Au nanomembrane was stratified between the polymer layers. The XPS depth profile also showed that the regions of pure metal atomic percent (100% Au), which are separated by the fluorine-rich layer, were observed (Figure 3g). The non-reactive surfaces are formed by the closely arranged fluorine atoms, which have a high electronegativity, around the carbon atoms.[37] Under the HIU irradiation, the stratified Au particles were unable to maintain their initial distribution and were easily displaced by the acoustic pressure. Optical microscope images, before and after HIU irradiation, demonstrated that the intermixed Au particles on SEBS formed reversible micro-cracks, maintaining their morphology intact even after HIU irradiation (Figure S11, Supporting Information).[38] The stratified Au particles on PFA represented irreversible micro-cracks, indicating the formation of defects on the top electrode under ultrasound irradiation.

We fabricated US-TENGs with both intermixed Au electrodes (intermixed structure) and stratified Au electrodes (stratified structure) to check their durability. Figure 3h shows simple schematics of each structure and their compact electrical model (Details in Note S2; Figure S12, Supporting Information). The electrical characteristics analysis using an LCR meter revealed that both structures initially formed a complete capacitor structure ($\approx$90° phase angle) and showed comparable impedance (stratified: 31.3 kΩ, intermixed: 31.6 kΩ) (Figure 3i). In contrast to the intermixed structure, the stratified structure exhibited a 9% decrease in capacitance and a 10% increase in impedance under HIU irradiation (Figure 3j; Figures S13 and S14, Supporting Information). This reduction can be attributed to defects in the top electrode, as previously discussed, leading to a diminished active area. This also led to a decrease in the current output in the stratified structure (Figure S15, Supporting Information). Furthermore, our findings suggest that the intermixed structure provides significant advantages in power efficiency and durability compared to previously reported structures with double-electrodes (Figure S16, Supporting Information).[21,27]

2.4. Sustainability and Biocompatibility of DUS-TENG

We characterized the electrical output of the fabricated DUS-TENG across various environments, focusing on its potential medical applications. In vitro, DUS-TENG generates an open-circuit voltage (V_{OC}) of 12.7 V and a short-circuit current (I_{SC}) of 0.301 mA, while in vivo it generates 10.1 V and 0.254 mA (Figures S17 and S18, Supporting Information). To assess the device's durability, we conducted accelerated aging experiments using HIU irradiation, similar to the methodology described in Figure 3. We irradiated the DUS-TENG with HIU for 500 seconds each cycle and checked the change in the device's output (**Figure 4a**). Despite the rigorous experimental conditions over six cycles, the device's electrical output remained stable. For the biocompatibility assessment, we evaluated the viability of CRL-1502 (human skin fibroblast) cells using the 3-(4,5-dimethylthiazol-2-yl)-2,5-diphenyltetrazolium bromide (MTT) assay. The results showed that, compared to the control group, the normalized viability of CRL-1502 cells exposed to DUS-TENG demonstrated no significant difference after 72 h (see Figure 4b). Furthermore, a Comet Assay was conducted to investigate the potential genotoxic effects of DUS-TENG, specifically its ability to cause DNA damage (Figure 4c). The findings indicated that the DUS-TENG did not induce DNA damage in CRL-1502 cells, as evidenced by no significant differences in DNA tail length compared to the control group (Figure 4d). To examine the inflammatory response following device implantation, we performed hematoxylin-eosin (H&E) staining on subdermal tissue at the site of implantation after three weeks (Figure 4e; Figure S19, Supporting Information). Over a period of three weeks, no significant inflammatory reaction was observed near the implanted sites when compared to the control group.

2.5. Simultaneous Wireless Information and Power Transfer using the DUS-TENG

To explore the simultaneous transmission of information and power, we developed an integrated system that combines a modulation circuit with the DUS-TENG, characterized by its long-term stability and high output. In the context of nerve stimulators, the efficacy of treatment on the same nerve varies depending on the stimulation protocol. Consequently, we introduced a battery-free, ultrasound-powered system capable of generating neurostimulation signals and offering feedback to adjust the stimulation protocol, aiming to treat a wide range of diseases.[39] To achieve this, we designed a system capable of pre-setting the conditions for nerve stimulation (amplitude, frequency, pulse width) and communicating these parameters to the DUS-TENG (**Figure 5a**; Figures S20–S23, Supporting Information). Initially, the controller sets the stimulation parameters, which are subsequently relayed to the transmitter. An ultrasound generator produces a continuous sinewave but modifies the signal timing based on the neurostimulation data, resulting in step-function ultrasound waves emitted by a transducer. The circuit, linked to the DUS-TENG, accumulates energy upon continuous ultrasound exposure but transitions to collecting nerve stimulation data upon receiving an initialization signal. This data
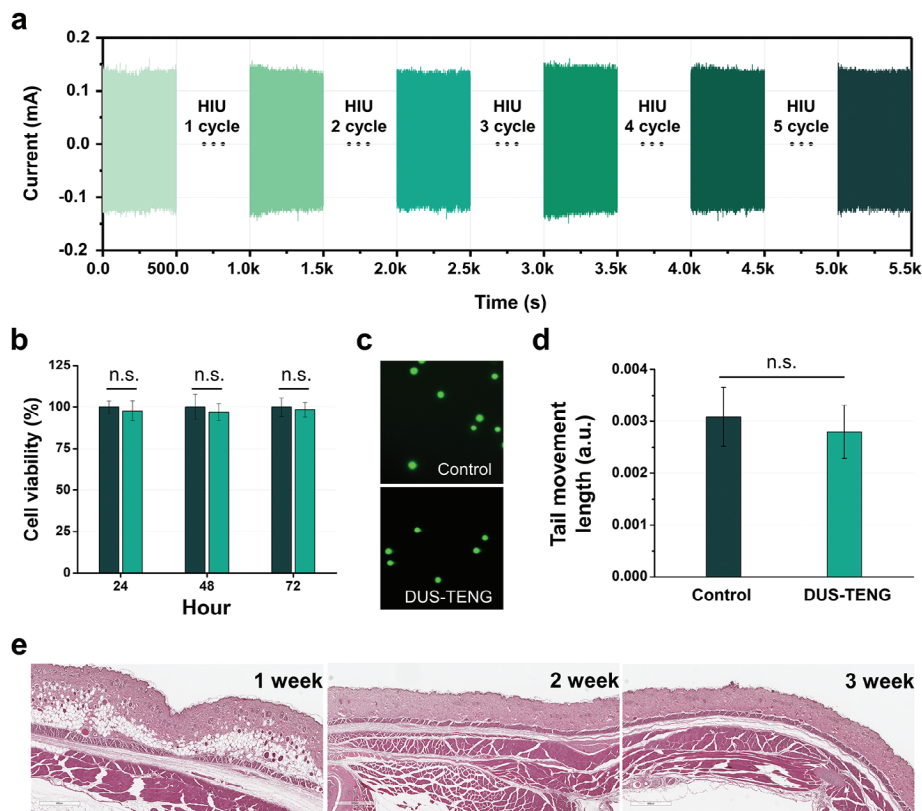
**ADVANCED
SCIENCE NEWS**

www.advancedsciencenews.com

**ADVANCED
ENERGY
MATERIALS**

www.advenergymat.de

Figure 4. Durability and biocompatibility of DUS-TENG. a) Long-term operation of the DUS-TENG. b) MTT assay result (n = 18 for each group). c) The fluorescent images obtained by comet assay of the DUS-TENG. d) The OTM graph from the comet assay result; n = 30 for each group. e) H&E-stained subdermal tissue image in implanted parts during 3-week implantation.

then informs adjustments to the nerve stimulation parameters, enabling targeted nerve activation via a cuff electrode.

We evaluated this simultaneous information and power transfer system within an in vivo environment (Figure 5b). Upon detecting the initialization signal for two steps (180 ms), the nerve stimulation circuit processes three types of information over an additional eight steps (120 ms). The initial two steps involve receiving amplitude information (ranging from 1 to 2 V), the subsequent two steps pertain to frequency data (from 2 to 10 Hz), and the next two steps focus on pulse width parameters (from 50 to 100 ms), and final two-steps consist of idle data bits. Activation of the nerve stimulation circuit is contingent upon this compiled information (Figure 5c). Our testing verified that the neurostimulation circuit accurately generates signals in response to adjustments in the neurostimulation settings (Figure 5d). Continuous ultrasound application preserves the altered nerve stimulation signal, whereas halting ultrasound transmission also ceases the nerve stimulation signal. Moreover, in the absence of transmitted initialization information, nerve stimulation signals remain active. Such an active nerve stimulation device enhances treatment efficacy, permitting adjustments in stimulation conditions based on feedback concerning the treatment's impact.

3. Conclusion

This work introduced a novel design strategy for the sustainable powering of the DUS-TENG, which enables the realization of a battery-free implant powered and controlled by ultrasound. FEA simulation and experimental results demonstrated that the double-electrode mode is essential to achieve high current output without the return gate effect. To ensure high and stable power generation, we designed the triboelectric membrane with a top electrode featuring Au nanoparticles intermixed within a self-adhesive SEBS layer. Material analysis using SEM-EDS and XPS techniques confirmed that the stability of the electrode under ultrasound is due to the intermixing properties. The entire device, encapsulated in SEBS, ensured biological safety, as demonstrated by in vivo and in vitro experiments using human fibroblasts, which is essential for long-term implantation. The DUS-TENG generates a sustained in vivo output sufficient to power the modulation circuit and transfer various acoustic signals, generating stimulation pulses with tunable parameters, including frequency, amplitude, and width, via acoustic signals. Ultrasound represents a promising energy source for transcutaneous power transfer that could replace conventional energy sources, and TENG has shown great promise for ultrasound energy harvesting. Challenges remain in achieving the diverse functions of implantable electronics-such as neurostimulation, sensing, pacing, and signal communication-solely through ultrasound. The DUS-TENG enables a multifunctional implant that can be both powered and modulated solely by an ultrasonic source. With continued development and optimization, it is expected that this work will be able to keep pace with advancements in next-generation battery-free implantable electronics.
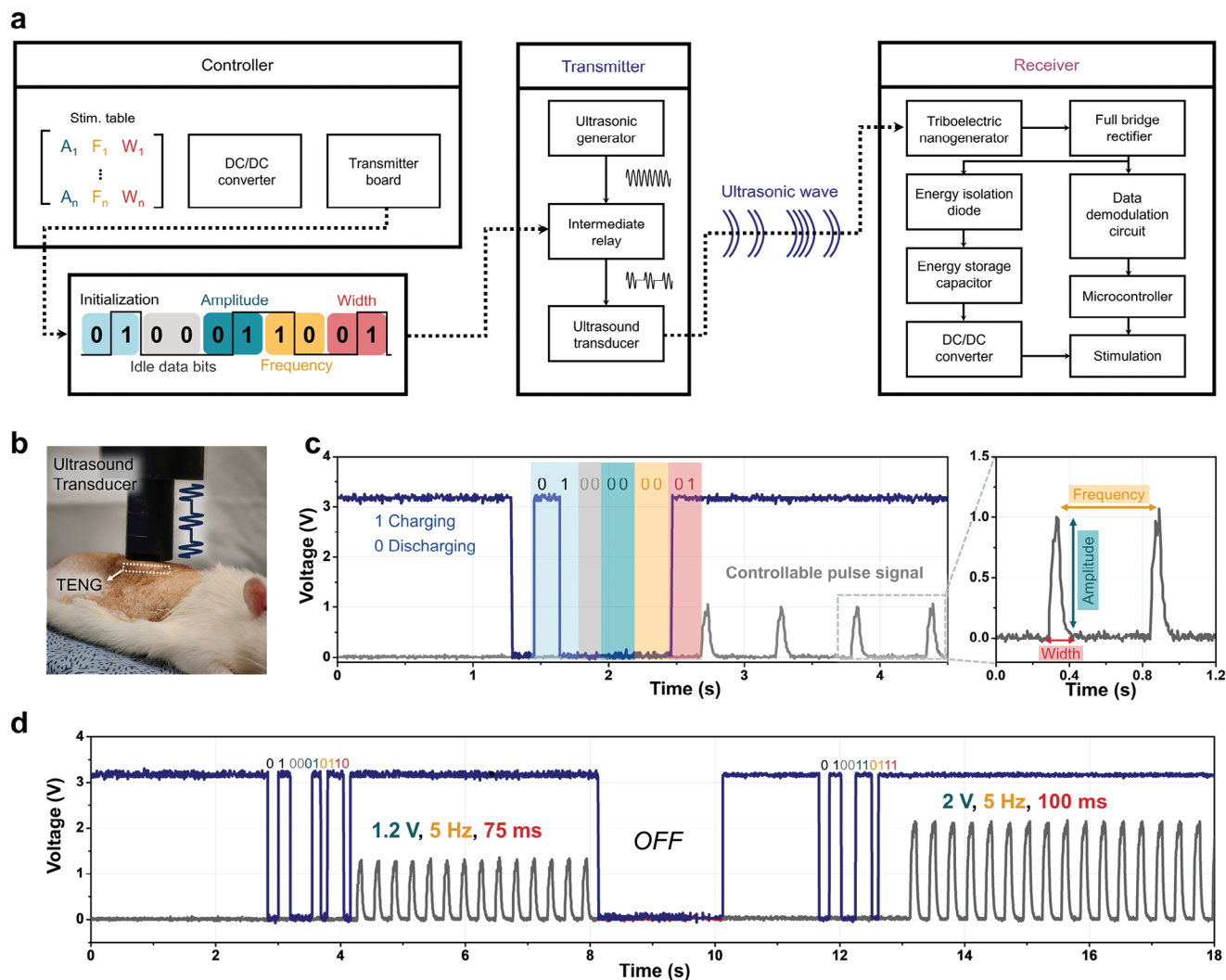
**ADVANCED
SCIENCE NEWS**

www.advancedsciencenews.com

**ADVANCED
ENERGY
MATERIALS**

www.advenergymat.de

Figure 5. Simultaneous wireless information and power transfer using the DUS-TENG. a) Block diagram of the simultaneous wireless information and power transfer system. b) In vivo test setup for the system. c) A graph illustrating the operation of the system that controls the amplitude, frequency, and width of the pulse signal. The neurostimulation circuit generates signals in response to adjustments in the neurostimulation settings. d) In vivo operation of the system.

4. Experimental Section

Materials Preparation: The fabrication process of the integrated membrane is described in Figure S2 (Supporting Information). PDMS was coated on a Si wafer as a supporting layer, which was then topped with a PFA film (ALPHAFLON, ≈25 µm). The hydrophilicity of the PFA film was enhanced by treating it with oxygen plasma. Then, trichloro(phenyl)silane was formed in the PFA through vapor treatment. A SEBS solution (Tuftec H1221, 15 wt.% in toluene) was spin-coated (1000 rpm, 60 s) on the as-prepared film and evaporated overnight in a fume hood at room temperature. The SEBS The Au nanoparticles were deposited on the SEBS film through an electron beam evaporator (0.05 nm s^{-1}, 45 nm thickness). The Au nanoparticles were connected to a copper wire using Ag paste. Another thick SEBS film for encapsulation was prepared through automatic bar coating and the same evaporation method above. The thick SEBS film covered the entire area by pressing. Finally, the fabricated integrated membrane was detached from the supporting layer.

Material Characterization: The microstructure of the integrated membrane was examined by obtaining cross-sectional films through ion milling (COXEM, CP 8000+). The FE-SEM (HITACHI, SU 5000) and EDS measurements were performed to analyze the cross-sectional image. T-peeling tests were performed to measure the adhesion strength using a universal testing machine (INSTRON, 3400 series). The test velocity was set to 0.5 mm s^{-1} and the peel strength was calculated as the average over 10–50 mm of deformation. XPS depth profiling (ThermoFisher, NEXSA) was performed to confirm the distribution of the Au nanoparticles. Au was deposited on SEBS or PFA using an electron beam evaporator, and the distribution was measured before and after ultrasound irradiation. The displacement amplitudes of the membrane were measured using a laser vibrometer (Polytec, CLV-2534). The detailed experimental setup for the displacement measurement is presented in Figure S4 (Supporting Information).

Device Fabrication: The device fabrication process is described in Figure S3 (Supporting Information). The integrated circuit (Figure S15, Supporting Information) was connected to a cuff electrode. Then, the

**ADVANCED
SCIENCE NEWS**

www.advancedsciencenews.com

**ADVANCED
ENERGY
MATERIALS**

www.advenergymat.de

integrated circuit was placed on the as-prepared integrated membrane. The copper wire on the membrane was connected to the circuit's input terminals, and the PCB and membrane were bonded together with a hot-melt adhesive. The entire device was finally sealed with SEBS.

Electrical Characterization: An LCR meter (Rohde & Schwarz, LCX 200) was used to analyze the electrical impedance of the TENG device. Voltage signals were measured using a digital phosphor oscilloscope (Keysight, MSOX3054T) with a voltage probe (Keysight, N2843A) of 10 MΩ input impedance. Current signals were measured using a low-noise current preamplifier (Stanford Research Systems, SR570). The low-frequency motion was applied using a pushing tester (Z-Tech, ZPS-100) to test the conventional TENG's output. Ultrasound generation and characterization were carried out using a commercial ultrasound transducer and generator (Mirae MV100).

Biocompatibility Analysis: For the MTT assay, human fibroblasts (ATCC, CRL–1502; Designation: WS1) and culture medium were added to each well of a 96-well plate containing 3×3 mm experimental samples (10 000 cells well^{-1}, final volume: 100 µL). The fibroblasts were then incubated for 24, 48, and 72 h. The culture medium was subsequently removed from the 96-well plates. Then, 50 µL of serum-free medium and 50 µL of MTT solution (Abcam, 5 mg mL^{-1}) were added to each well. The plate was incubated at 37 °C for 2 h. Next, the serum-free medium and the MTT solution were removed. The samples were cleaned by rinsing them with diluted PBS solution. Finally, 150 µL of a solubilizing agent (dimethyl sulfoxide, Sigma–Aldrich) was added to dissolve the formazan crystals for 15 min. Finally, 100 µL of the solution was transferred to another 96-well plate, and the absorbance was measured at OD = 590 nm. To conduct the comet assay, we prepared a lysis buffer (Thermo Fisher Scientific), an alkaline solution (SAMCHUN Chemical), and a tris-borate ethylene-diamine-tetraacetic acid (TBE) electrophoresis solution (Thermo Fisher Scientific). The agarose gel was melted until it became liquefied, and 75 µL of the agarose gel was added to the slide to form the base layer. The slide was then kept at 4 °C for 15 min. A mixture of human fibroblasts and agarose gel in a 1:10 ratio was transferred onto the base layer using 75 µL of the mixture. The slide was kept at 4 °C for 15 min. Subsequently, the slide was immersed sequentially in pre-chilled lysis buffer (25 mL) for 60 min, alkaline solution (25 mL) for 30 min at 4 °C in dark conditions, and TBE electrophoresis solution for 10 min, while maintaining the required temperature and darkness. For the electrophoresis procedure, the chamber was filled with cold TBE electrophoresis solution until the slides were completely covered. An electric field of 0.1 V mm^{-1} was applied for 15 min. Following electrophoresis, the slide was rinsed three times with pre-chilled deionized water and a 70% ethanol solution. Once dry, 100 µL of diluted Vista Green DNA dye was added to the slide, and it was incubated for 15 min at room temperature. Finally, the olive tail moment (OTM) was measured by observing the slide using epifluorescence microscopy with a FITC filter. The anesthesia and implantation of the neurostimulator were carried out using the aforementioned procedures. Subdermal tissue from the implanted area was harvested at the desired time points and observed for inflammation using hematoxylin and eosin staining (H&E staining).

Circuit Operation: The integrated device was positioned 10 mm below the ultrasound probe. Then, fill the space between the TENG and the ultrasound probe with an appropriate amount of ultrasound coupling agent. The oscilloscope was connected to the voltage detection ports of the energy storage capacitor and pulse output ports. As ultrasound was irradiated on the device, the oscilloscope parameters should be observed until the voltage across the storage capacitor no longer rises significantly. Messages are sent through the message-sending software. The microprocessor receives computer transmitter information, including pulse frequency, pulse width, and other necessary information, through the RS-422 bus. It generates an ultrasound signal modulation signal using on-off keying modulation. The modulation signal passes through an optocoupler isolator and MOS tube to control the intermediate relay input voltage. This, in turn, controls the opening and closing of the intermediate relay output contacts, which controls the ultrasound transducer drive signal. The circuit information demodulation module processes this information to produce a 0/1 signal, which is identified by the STM32L0 microcontroller. Finally, the STM32L0 utilizes the acquired information to generate

corresponding pulses through the pulse width modulation (PWM) function of the microcontroller and the filter circuit. The resulting output was recorded and saved using a digital storage oscilloscope. Message sending software on PC written in VB language. For an in vivo demonstration, healthy adult male Sprague–Dawley rats (weight: (250−450) g; age: 8−11 weeks; bred and distributed by Orient Bio, Rep. of Korea) were prepared and performed in the same manner as described above. This study was reviewed and approved by the Institutional Animal Care and Use Committee (IACUC) of Samsung Medical Center (20230421001).

Supporting Information

Supporting Information is available from the Wiley Online Library or from the author.

Conflict of Interest

The authors declare no conflict of interest.

Data Availability Statement

The data that support the findings of this study are available from the corresponding author upon reasonable request.

[1] V. Nair, A. N. Dalrymple, Z. Yu, G. Balakrishnan, C. J. Bettinger, D. J. Weber, K. Yang, J. T. Robinson, *Science* **2023**, *382*, eabn4732.

[2] H. Sheng, X. Zhang, J. Liang, M. Shao, E. Xie, C. Yu, W. Lan, *Adv. Healthcare Mater.* **2021**, *10*, 2100199.

[3] H. Guo, W. Bai, W. Ouyang, Y. Liu, C. Wu, Y. Xu, Y. Weng, H. Zang, Y. Liu, L. Jacobson, Z. Hu, Y. Wang, H. M. Arafa, Q. Yang, D. Lu, S. Li, L. Zhang, X. Xiao, A. Vazquez-Guardado, J. Ciatti, E. Dempsey, N. Ghoreishi-Haack, E. A. Waters, C. R. Haney, A. M. Westman, M. R. MacEwan, M. A. Pet, J. A. Rogers, *Nat. Commun.* **2022**, *13*, 3009.

[4] S. M. Won, L. Cai, P. Gutruf, J. A. Rogers, *Nat. Biomed. Eng.* **2023**, *7*, 405.

[5] C. Y. Kim, M. J. Ku, R. Qazi, H. J. Nam, J. W. Park, K. S. Nam, S. Oh, I. Kang, J.-H. Jang, W. Y. Kim, J.-H. Kim, J.-W. Jeong, *Nat. Commun.* **2021**, *12*, 535.

[6] S. K. Karan, S. Maiti, J. H. Lee, Y. K. Mishra, B. B. Khatua, J. K. Kim, *Adv. Funct. Mater.* **2020**, *30*, 2004446.

[7] Z. Liu, H. Li, B. Shi, Y. Fan, Z. L. Wang, Z. Li, *Adv. Funct. Mater.* **2019**, *29*, 1808820.

[8] D. Jiang, B. Shi, H. Ouyang, Y. Fan, Z. L. Wang, Z. Li, *ACS Nano* **2020**, *14*, 6436.

[9] Q. Zheng, Y. Zou, Y. Zhang, Z. Liu, B. Shi, X. Wang, Y. Jin, H. Ouyang, Z. Li, Z. L. Wang, *Sci. Adv.* **2016**, *2*, 1501478.

[10] X. Pu, S. An, Q. Tang, H. Guo, C. Hu, *Iscience* **2021**, *24*, 102027.

[11] Q. Zheng, B. Shi, F. Fan, X. Wang, L. Yan, W. Yuan, S. Wang, H. Liu, Z. Li, Z. L. Wang, *Adv. Mater.* **2014**, *26*, 5851.

[12] Y.-J. Kim, J. Lee, J.-H. Hwang, Y. Chung, B.-J. Park, J. Kim, S.-H. Kim, J. Mun, H.-J. Yoon, S.-M. Park, S.-W. Kim, *Adv. Mater.* **2024**, *36*, 2307194.

[13] C. Chen, Z. Wen, J. Shi, X. Jian, P. Li, J. T. Yeow, X. Sun, *Nat. Commun.* **2020**, *11*, 4143.

[14] W. J. Tomlinson, S. Banou, C. Yu, M. Stojanovic, K. R. Chowdhury, *IEEE Commun. Surv. Tutor.* **2018**, *21*, 1145.

[15] J. Li, Y. Dong, J. H. Park, J. Yoo, *Nat. Electron.* **2021**, *4*, 530.

[16] I. Mayordomo, T. Dräger, P. Spies, J. Bernhard, A. Pflaum, *Proc. IEEE* **2013**, *101*, 1302.

[17] F. T. Alrashdan, J. C. Chen, A. Singer, B. W. Avants, K. Yang, J. T. Robinson, *J. Neural. Eng.* **2021**, *18*, 045011.

[18] M. Li, Y. Song, Y. Hou, N. Li, Y. Jiang, M. Sulaman, Q. Hao, *IEEE T. Biomed. Circ. S.* **2019**, *13*, 1747.

[19] D. Liu, L. Zhou, S. Cui, Y. Gao, S. Li, Z. Zhao, Z. Yi, H. Zou, Y. Fan, J. Wang, Z. L. Wang, *Nat. Commun.* **2022**, *13*, 6019.

[20] T. Kim, H. Yong, B. Kim, D. Kim, D. Choi, Y. T. Park, S. Lee, *Nat. Commun.* **2018**, *9*, 1437.

[21] X. Liu, Y. Wang, G. Wang, Y. Ma, Z. Zheng, K. Fan, J. Liu, B. Zhou, G. Wang, Z. You, Y. Fang, X. Wang, S. Niu, *Matter* **2022**, *5*, 4315.

[22] W. Deng, A. Libanori, X. Xiao, J. Fang, X. Zhao, Y. Zhou, G. Chen, S. Li, J. Chen, *Nano Energy* **2022**, *91*, 106656.

[23] G. Yao, L. Kang, J. Li, Y. Long, H. Wei, C. A. Ferreira, J. J. Jeffery, Y. Lin, W. Cai, X. Wang, *Nat. Commun.* **2018**, *9*, 5349.

[24] R. Hinchet, H.-J. Yoon, H. Ryu, M.-K. Kim, E.-K. Choi, D.-S. Kim, S.-W. Kim, *Science* **2019**, *365*, 491.

[25] S. Niu, Y. Liu, S. Wang, L. Lin, Y. S. Zhou, Y. Hu, Z. L. Wang, *Adv. Funct. Mater.* **2014**, *24*, 3332.

[26] B. Kim, H.-J. Yoon, Y.-J. Kim, B.-J. Park, J.-H. Jung, S.-W. Kim, *ACS Energy Lett.* **2023**, *8*, 3412.

[27] H. S. Kim, S. Hur, D.-G. Lee, J. Shin, H. Qiao, S. Mun, H. Lee, W. Moon, Y. Kim, J. M. Baik, C.-Y. Kang, J. H. Jung, H.-C. Song, *Energy & Environ. Sci.* **2022**, *15*, 1243.

[28] A. Fedotchev, S. Parin, S. Polevaya, A. Zemlianaia, *J. Pers. Med.* **2021**, *11*, 437.

[29] S. Zanos, *Perspect. Med.* **2019**, *9*, a034314.

[30] Y. Jiang, S. Ji, J. Sun, J. Huang, Y. Li, G. Zou, T. Salim, C. Wang, W. Li, H. Jin, J. Xu, S. Wang, T. Lei, X. Yan, W. Y. Peh, S.-C. Yen, Z. Liu, M. Yu, H. Zhao, Z. Lu, G. Li, H. Gao, Z. Liu, Z. Bao, X. Chen, *Nature* **2023**, *614*, 456.

[31] Y. Ohkubo, K. Endo, K. Yamamura, *Sci. Rep.* **2018**, *8*, 18058.

[32] N. Inagaki, K. Narushima, T. Yamamoto, *J. Appl. Polym. Sci.* **2002**, *85*, 1087.

[33] J. Shao, M. Willatzen, Z. L. Wang, *J. Appl. Phys.* **2020**, *128*, 111101.

[34] J. Shao, T. Jiang, Z. L. Wang, *Sci. China Technol. Sci.* **2020**, *63*, 1087.

[35] D.-M. Lee, N. Rubab, I. Hyun, W. Kang, Y.-J. Kim, M. Kang, B. O. Choi, S.-W. Kim, *Sci. Adv.* **2022**, *8*, eabl8423.

[36] ISO 14708-1, Implants for surgery – Active implantable medical devices – Part 1: General requirements for safety, marking and for information to be provided by the manufacturer, **2014**.

[37] E. David, A. Lazar, A. Armeanu, *J. Mater. Process. Technol.* **2004**, *157*, 284.

[38] J. Y. Oh, D. Son, T. Katsumata, Y. Lee, Y. Kim, J. Lopez, H.-C. Wu, J. Kang, J. Park, X. Gu, J. Mun, N. G.-J. Wang, Y. Yin, W. Cai, Y. Yun, J. B.-H. Tok, Z. Bao, *Sci. Adv.* **2019**, *5*, eaav3097.

[39] D. Adair, D. Truong, Z. Esmaeilpour, N. Gebodh, H. Borges, L. Ho, J. D. Bremner, B. W. Badran, V. Napadow, V. P. Clark, *Brain Stimul.* **2020**, *13*, 717.